Energy Conversion and Management: X 27 (2025) 101183

Contents lists available at ScienceDirect

Energy Conversion and Management: X

journal homepage: www.sciencedirect.com/journal/energy-conversion-and-management-x

A convolutional neural network driven suspension control strategy to enhance sustainability of high-speed trains

Duo Zhang [a,1], Hong-Wei Li [b,*], Fang-Ru Zhou [c,1], Yin-Ying Tang [c,d], Qi-Yuan Peng [c,d]

[a] Department of Mechanical Engineering, Politecnico di Milano, Milan, Italy
[b] Department of Civil and Environmental Engineering, The Hong Kong Polytechnic University, Hong Kong, People's Republic of China
[c] School of Transportation & Logistics, Southwest Jiaotong University, Chengdu, People's Republic of China
[d] National Engineering Laboratory of Integrated Transportation Big Data Application Technology, Southwest Jiaotong University, Chengdu, People's Republic of China

ARTICLE INFO

Keywords:
High-speed train
Energy efficiency
Riding comfort
Suspension control
Convolutional neural network
Bi-objective optimization

ABSTRACT

With the accelerated expansion of rail networks and the increase in operation speeds, railway undertakings are under considerable pressure to curtail energy consumption of high-speed trains to achieve sustainability goals, while still maintaining passenger satisfaction. For addressing this challenge, a convolutional neural network driven control strategy is proposed for the suspension system of high-speed vehicles to simultaneously reduce energy consumption and carbody vibration on curved tracks. Firstly, a co-simulation platform is established between the multibody dynamics simulation software and MATLAB/Simulink, and a series of running conditions are designed. Based on the co-simulation results, the roles that train's velocity, track curvature, and scale factor of the Skyhook controller play in energy efficiency and lateral carbody vibration are systematically studied. Subsequently, a convolutional neural network is constructed based on the simulation data to predict the energy consumption and riding comfort under complex operation scenarios. In conjunction with the neural network algorithm, a bi-objective optimization model is further developed and solved to adjust scale factor of the Skyhook controller according to different running conditions. The optimization results indicate that energy consumption and lateral vibration of a high-speed train on curved tracks can be respectively reduced by up to 15.90 % and 47.78 % through employment of the proposed control strategy.

1. Introduction

In recent decades, the high-speed railway (HSR) has been intensively developed by many countries to effectively enhance national and regional accessibility as the link between cities [1]. While HSR has a great reputation for safety, celerity, and punctuality, the rising speed poses significant challenges for its sustainability, particularly in terms of energy efficiency and passenger comfort [2].

Compared with road and aviation, the railway is a more environment-friendly transport mode [3]. However, the energy consumption of HSR increases significantly because the rising vehicle speed will aggravate the mechanical resistances, which can consume up to 30 % of the traction energy [4]. It is critical to take effective measures to decrease the energy consumed by motion resistance (ECMR) for high-speed trains (HST). Furthermore, with the development of HSR, people have higher requirements for the riding comfort [5]. The lateral carbody vibration on the curved track should be specifically paid attention to because it will bring more inconvenience to the passengers with the joint action of centrifugal force. Thus, an energy-efficient and comfortable HST is needed to benefit the environment and passengers.

Currently, there are three methods extensively employed to decrease the ECMR of HST: optimizing the train operation control strategy (TOCS), weakening the wind drag force, and vehicle mass reduction. Howlett et al. [6] regarded the train as a mass point to optimize the schedule of accelerating, cruise, coasting, and braking for decreasing ECMR. Subsequently, different mathematical models and algorithms were proposed to investigate the energy-efficiency TOCS [7–10]. Because the wind resistance will consume a lot of energy when the vehicle speed is high, the train composition, shape of train's head, and nose length were optimized to weaken the wind drag force [11]. In order to decrease the motion resistance, kinds of lightweight materials were employed to manufacture the railway vehicle. Mistry et al. [12] used the

* Corresponding author.
E-mail address: hong-wei.li@polyu.edu.hk (H.-W. Li).
[1] These authors contributed equally to this work and should be considered co-first authors.

https://doi.org/10.1016/j.ecmx.2025.101183
Received 1 May 2025; Received in revised form 23 July 2025; Accepted 2 August 2025
Available online 5 August 2025

fibre reinforced polymer composite materials to identify key components for lightweighting of a rail vehicle. Carruthers et al. [13] proposed a systematic approach to select materials that match the design requirements and constraints of a given application. All these strategies can play a positive role in improving the energy efficiency of HST, but they have few effects or even negative effects on riding comfort.

Apart from the mentioned commonly used methods, Zhang et al. [14] demonstrated that nearly 4 % ECMR can be reduced through optimizing suspension damping coefficients. Obviously, adjusting suspensions has a direct effect on riding comfort because the suspension is the primary component of HST for restraining the carbody vibration. Thus, it is challenging and meaningful to realize the bi-objective optimization for energy efficiency and vibration isolation when improving suspensions.

For the sake of better shock absorption performance, kinds of active and semi-active control strategies have been applied to suspensions. The active control strategy has the shortcomings of high energy consumption and high cost [15]. Thus, in this research, we prefer to adopt the semi-active control strategy which can adjust the damping forces according to signals picked up by the sensors with very little external energy [16].

In recent years, different types of semi-active control strategies have been proposed [17–20]. Among which, elementary semi-active control strategy of Skyhook is the most widely used pattern [20], leading to successful practical applications in different countries, e.g. Germany [21] and Japan [22]. Due to its simplicity and efficiency, Skyhook controllers were employed for secondary lateral dampers (SLDs) [23], secondary vertical dampers (SVDs) [24], yaw dampers (YDs) [25], and primary vertical dampers (PVDs) [26], as is shown in Fig. 1. In this paper, we plan to improve the lateral riding comfort of HST as mentioned in the **Introduction**. Thus, the SLD will be focused on.

The ideal Skyhook control strategy supposes that a virtual damper exists between the carbody and a virtual wall for constraining the lateral acceleration of carbody, as illustrated in Fig. 2, where y_b and y_s denote the lateral displacement of the carbody and sideframe respectively, C denotes the damping coefficient of SLD. But actually, we have to make use of SLD to achieve Skyhook control strategy.

To be specific, the Skyhook control strategy is generally divided into two types, as described in Eqs. (1) and (2), where C_{max} and C_{min} respectively represent the maximum and minimum damping coefficients generated by SLD, cs represents the ideal damping coefficient of the virtual Skyhook damper [27]. Since the on–off version has a poor performance at high frequencies, we adopt the continuous Skyhook control strategy to address this issue [28].

On-off Skyhook:

$$C = \begin{cases} C_{max} & \dot{y}_b \bullet (\dot{y}_b - \dot{y}_s) \geq 0 \\ C_{min} & \dot{y}_b \bullet (\dot{y}_b - \dot{y}_s) < 0 \end{cases} \tag{1}$$

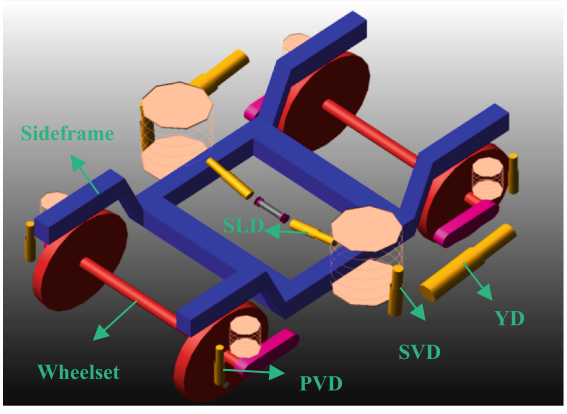

Fig. 1. The dampers of a bogie.

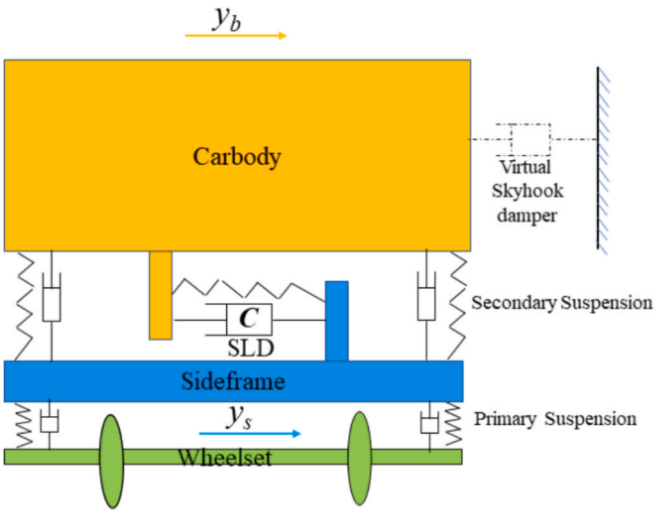

Fig. 2. Schematic diagram of Skyhook control.

Continuous Skyhook:

$$C = \begin{cases} C_{max} & cs\dfrac{\dot{y}_b}{\dot{y}_b - \dot{y}_s} \geq C_{max} \\ cs\dfrac{\dot{y}_b}{\dot{y}_b - \dot{y}_s} & C_{min} < cs\dfrac{\dot{y}_b}{\dot{y}_b - \dot{y}_s} < C_{max} \\ C_{min} & cs\dfrac{\dot{y}_b}{\dot{y}_b - \dot{y}_s} \leq C_{min} \end{cases} \tag{2}$$

Because the values of C_{max} and C_{min} depend on the property of the damper, cs obviously has a critical effect on the performance of the semi-active control. For better expression cs is usually evaluated by a scale factor (k), which is the ratio between cs and C_{max}. In terms of passenger comfort, Wu et al. [20] and Zhao et al. [23] assigned k as 1, while Oh et al. [29] adopted 1.6 as the value of k. However, these values were typically determined through trial and error, relying on empirical judgment rather than systematic optimization, which may not yield the most effective vibration control. We argue that k should instead be a variable parameter, dynamically adjusted in response to real-time vehicle operating conditions. Yet, due to the inherent nonlinearity of the wheel-rail coupling system, achieving real-time adjustment of k remains a challenge.

Recent advancements in deep learning have opened new avenues for suspension control, particularly in addressing nonlinearities and uncertainties inherent in dynamic systems [30]. Konolko et al. [31] formulated a deep neural network controller for active suspension systems. The automated structure search method identified a six-layer deep neural network with mixed activation functions as optimal. The experimental validation demonstrated a 4 % reduction in sprung mass acceleration when compared to conventional PID control. Zhang and Ji [32] developed a high-stability control strategy for magnetic suspension systems. This strategy employed the convolutional neural network (CNN) to facilitate adaptive PID parameter tuning. The efficacy of the proposed method was evidenced in addressing rotor stability under four typical driving conditions. Li et al. [33] introduced a CNN-based model for predicting the suspension gap of high-speed maglev trains. It innovatively integrated graph convolutional networks with gated recurrent units to effectively process spatiotemporal sequence data. Experimental results showed that the CNN model outperformed the LSTM baseline, achieving a 5.7 % increase in accuracy. Ye et al. [34] designed a 1D CNN-based fault diagnostic method for the suspension system of the high-speed train. To enhance the robustness of the method, the Gaussian white noise strategy and the edge sample training strategy were both adopted for immunity to track irregularities and wheel wear. The

1DCNN model was further validated using the tracking data of a CRH3 train. Sun and Cong [35] presented a deep learning-based road recognition framework for intelligent suspension systems, with the objective of optimizing vehicle comfort and stability. The proposed framework incorporated the semi-active suspension model with magneto-rheological dampers, leveraging CNN for real-time road classification. Simulation results indicated that the control strategy can significantly improve the suspension performance. These studies underscore the effectiveness of deep learning techniques in optimizing suspension systems, providing a robust framework for tackling complex control challenges in high-speed trains. However, current research primarily focuses on utilizing deep learning algorithms to predict and optimize the dynamic performance of suspension systems, while the relationship between suspension control and vehicle energy consumption remains underexplored. Given that the interactions between suspension control and vehicle energy consumption also involve complicated nonlinear mechanisms, deep learning-based modeling and optimization approaches can offer substantial potential for characterizing these interactions and developing more efficient control strategies.

Moreover, the establishment of an effective indicator system is a critical prerequisite for parameter optimization. Previous studies have primarily focused on ride comfort and safety metrics in semi-active suspension design: Jin et al. [36] developed a versatile semi-active suspension system targeting improved ride comfort, quantified by carbody acceleration in the global coordinate system. Similarly, Liao et al. [37] assessed various semi-active control strategies using a ride index derived from carbody accelerations, while Zhao et al. [23] proposed a coordination control strategy to enhance both running safety (evaluated via derailment coefficient) and ride comfort (measured by carbody acceleration) compared to the passive control. However, these studies notably omitted energy consumption during curve negotiation as a performance metric.

Building on these foundations, we propose an intelligent control strategy which can adjust the value of k automatically for better energy efficiency and ride comfort, assisting society in achieving carbon neutrality and providing a superior passenger experience. The main contributions of this work can be summarized as follows:

(1) While numerous studies have developed various semi-active control strategies for HSTs, most have overlooked two critical aspects: the influence of these control strategies on energy consumption, and the impact of varying running conditions on strategy effectiveness. To address these gaps, this study employs multibody dynamics (MBD) simulations to systematically evaluate how the scale factor affects both carbody acceleration and ECMR under different operational scenarios. The findings provide a foundational basis for optimizing semi-active control strategies to simultaneously enhance ride comfort and energy efficiency.
(2) Existing research integrating suspension control strategies for HSTs with deep learning techniques has predominantly concentrated on single-objective optimization and lacks investigation of energy efficiency metrics. This study overcomes this deficit by proposing a CNN-based predictive model to capture the nonlinear relationships between the scale factor, ECMR, and carbody acceleration across diverse operational scenarios. The CNN model enables accurate real-time predictions and establishes the foundation for the multi-objective optimization framework that dynamically balances energy savings and vibration reduction. This comprehensive approach advances semi-active suspension control beyond empirical methods by combining data-driven modeling with adaptive optimization. This would further enhance the sustainability and intelligence of modern suspension systems.

The following parts are structured: Section 2 establishes a co-simulation platform which can realize Skyhook control for SLD of HST and evaluate the energy efficiency and riding comfort of HST during operations. Section 3 demonstrates the effects of k on the energy consumption and lateral carbody vibration of HST according to simulation results and optimizes the value of k by convolutional neural network (CNN) and the non-dominated sorting genetic algorithm (NSGA-II). Conclusions are drawn in Section 4.

2. Methodology

2.1. Multibody dynamics model of high-speed trains

MBD simulation is a popular method when optimizing the parameters of the railway vehicle because it is low-cost, accurate, and convenient [38]. In this paper, the MBD model of HST is built by VI-Rail. As illustrated by Fig. 3, the vehicle is mainly made up of carbody, two sideframes, and four wheelsets. The notations of the symbols in Fig. 3 are given in Table 1. Each component of the vehicle has five DOFs: the vertical displacement, the lateral displacement, the roll angle, the yaw angle, and the pitch angle. All these components are connected by different kinds of joints and constraints. The primary suspension can decrease the relative vibration between the sideframe and wheelset, and the secondary suspension can restrain the movement of carbody.

As the train operates, carbody vibrations respond directly to the external forces and moments applied. These load conditions are illustrated in Fig. 4, and described in Table 2. Based on the Newton's second law, the motion equations of the carbody can be formulated.

- Lateral motion:

$$M_c\left[\ddot{Y}_c+\frac{v^2}{R_c}+(r_0+H_{cs}+H_{sf}+H_{fw})\ddot{\phi}_{\mathrm{sec}}\right] = F^L_{ys1}+F^L_{ys2}+F^R_{ys1}+F^R_{ys2}+M_c g\phi_{\mathrm{sec}} \tag{3}$$

- Vertical motion:

$$M_c(\ddot{Z}_c-a_0\ddot{\phi}_{\mathrm{sec}}-\frac{v^2}{R_c}\phi_{\mathrm{sec}}) = -F^L_{zs1}-F^L_{zs2}-F^R_{zs1}-F^R_{zs2}+M_c g \tag{4}$$

- Roll motion:

$$I_{cx}\left(\ddot{\phi}_c+\ddot{\phi}_{\mathrm{sec}}\right) = -\left(F^L_{ys1}+F^L_{ys2}+F^R_{ys1}+F^R_{ys2}\right)H_{cs}+\left(F^L_{zs1}+F^L_{zs2}-F^R_{zs1}-F^R_{zs2}\right)d_s-M_{r1}-M_{r2} \tag{5}$$

- Pitch motion:

$$I_{cy}\ddot{\beta}_c = (F^L_{zs1}+F^R_{zs1}-F^L_{zs2}-F^R_{zs2})l_c-\left(F^L_{xs1}+F^L_{xs2}+F^R_{xs1}+F^R_{xs2}\right)H_{cs}-\left(F^L_{xa1}+F^L_{xa2}+F^R_{xa1}+F^R_{xa2}\right)H_{cs} \tag{6}$$

- Yaw motion:

$$I_{cz}\left[\ddot{\psi}_c+v\frac{d}{dt}\left(\frac{1}{R_c}\right)\right] = \left(F^L_{ys1}+F^R_{ys1}-F^L_{ys2}-F^R_{ys2}\right)l_c+\left(F^R_{xs1}+F^R_{xs2}-F^L_{xs1}-F^L_{xs2}\right)d_s+\left(F^R_{xa1}+F^R_{xa2}-F^L_{xa1}-F^L_{xa2}\right)d_{sc} \tag{7}$$

The definitions of emerging symbols from Eq. (3) to Eq. (7) are listed in Table 3.

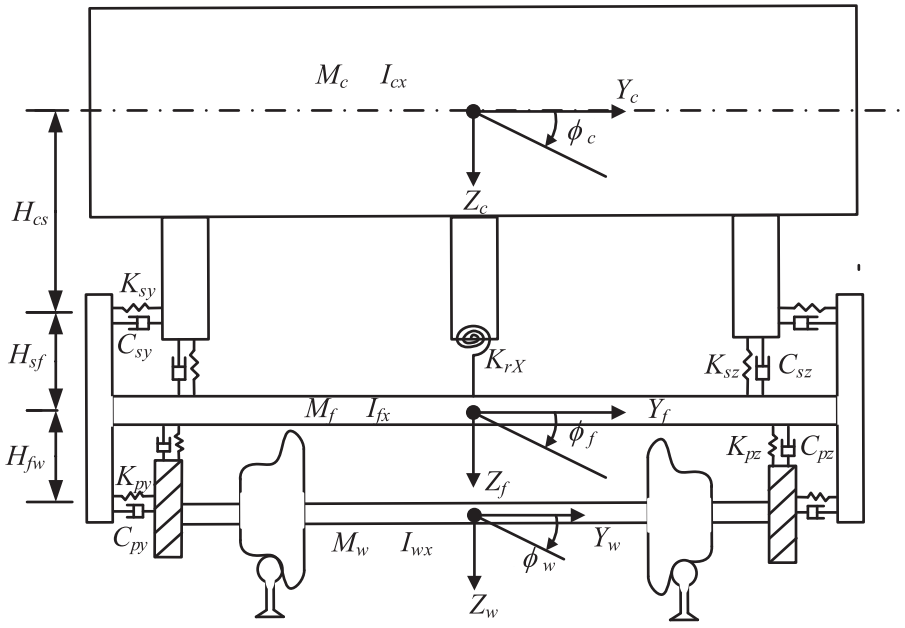

Fig. 3. Schematic diagram of the vehicle.

Table 1
Notations for parameters of the vehicle model.

Notation	Physical meaning
Y_c, Y_f, Y_w	Lateral displacements of carbody, sideframe, and wheelset
Z_c, Z_f, Z_w	Vertical displacements of carbody, sideframe, and wheelset
ϕ_c, ϕ_f, ϕ_w	The roll angles of carbody, sideframe, and wheelset
M_c, M_f, M_w	The masses of carbody, sideframe, and wheelset
I_{cx}, I_{fx}, I_{wx}	Mass moment of inertia of carbody, sideframe, and wheelset about X-axis
K_{py}, K_{sy}	Lateral stiffness coefficients of primary and secondary suspensions
K_{pz}, K_{sz}	Vertical stiffness coefficients of primary and secondary suspensions
C_{py}, C_{sy}	Lateral damping coefficients of primary and secondary suspensions
C_{pz}, C_{sz}	Vertical damping coefficients of primary and secondary suspensions
K_{rX}	Stiffness coefficient of anti-roll spring
H_{cs}	Vertical distance from the center of carbody to the secondary suspension
H_{sf}	Vertical distance from the secondary suspension to the center of sideframe
H_{fw}	Vertical distance from the center of sideframe to the center of wheelset

Based on the dynamics analysis of the carbody and other related descriptions in [39], the established MBD model of HST is illustrated in Fig. 5, which utilizes a PID controller to enforce precise tracking of the target velocity during operation. The PID controller implements a sophisticated three-term control strategy to accurately regulate the traction force of HST in real-time. Its control strategy combines a proportional term (K_p) for immediate response to velocity errors, an integral term (K_i) to eliminate steady-state offset through continuous error integration, and a derivative term (K_d) to provide predictive damping and mitigate system oscillations [40]. The control law is mathematically expressed as

$$F_t(t) = K_p e(t) + K_i \int_0^t e(t)dt + K_d \frac{de(t)}{dt} \tag{8}$$

where F_t denotes the traction force, and $e(t)$ denotes the error between the target velocity and the actual velocity.

Thus, ECMR of HST can be calculated as

$$W = \int_0^t (F_t v)dt \tag{9}$$

The calculation function of Eq. (9) has been validated by the law of conservation of energy in [14] and utilized in [41].

The parameter values of the MBD model are set according to [42]. The German low-interference track irregularities are adopted as the external excitation of the railway vehicle, and their power spectral density (PSD) functions are as below [43].

- Vertical irregularity:

$$S_v(\Omega) = \frac{A_v \bullet \Omega_c^2}{(\Omega_c^2 + \Omega^2)(\Omega_r^2 + \Omega^2)} \tag{10}$$

- Lateral irregularity:

$$S_a(\Omega) = \frac{A_a \bullet \Omega_c^2}{(\Omega_c^2 + \Omega^2)(\Omega_r^2 + \Omega^2)} \tag{11}$$

- Cross irregularity:

$$S_c(\Omega) = \frac{(A_v/b^2)\Omega_c^2 \bullet \Omega^2}{(\Omega_c^2 + \Omega^2)(\Omega_r^2 + \Omega^2)(\Omega_s^2 + \Omega^2)} \tag{12}$$

where Ω is the spatial angular frequency; Ω_c, Ω_r, Ω_s are the truncation angular frequencies; A_a, A_v are the scalar factors; b is the half of the reference distance between the rails, usually equals to 0.75 m. The values of these parameters are shown in Table 4.

When the vehicle runs at 350 km/h along a tangent track, the lateral acceleration of the carbody is revealed in Fig. 6. It is observed that the peak value is around 0.5 m/s^2, indicating good agreement with field test results introduced in [42]. The accuracy of the MBD model is demonstrated.

2.2. Semi-active control model

Although the MBD software of VI-Rail can establish the vehicle model accurately, it is difficult to apply the Skyhook control strategy to the SLD by VI-Rail. Thus, the co-simulation platform based on VI-Rail

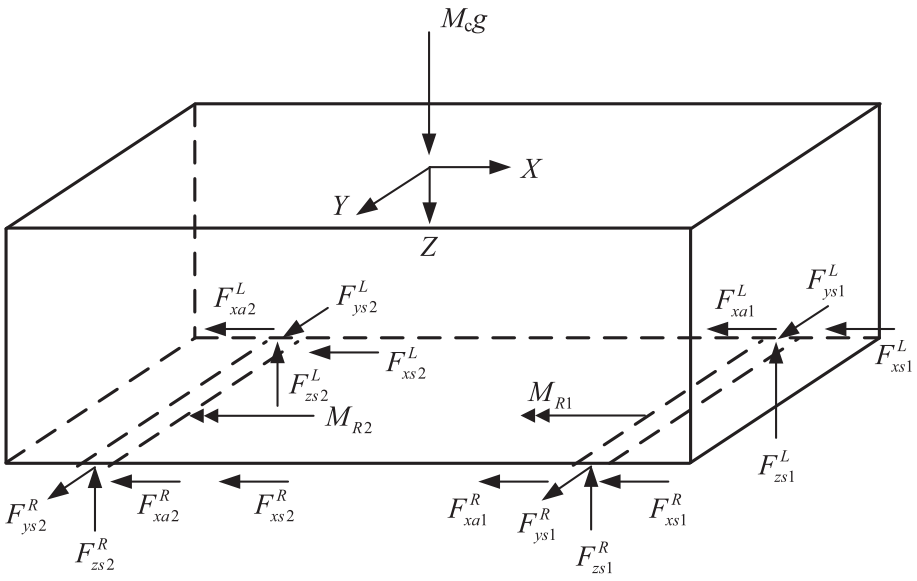

Fig. 4. Forces and moments on the carbody.

Table 2
Notations for forces in the carbody.

Notation	Physical meaning
F^L_{xsi}, F^R_{xsi}	Left and right longitudinal forces at secondary suspension of the *i*th bogie
F^L_{ysi}, F^R_{ysi}	Left and right lateral forces at secondary suspension of the *i*th bogie
F^L_{zsKi}, F^R_{zsKi}	Left and right vertical forces at secondary suspension of the *i*th bogie
F^L_{zsCi}, F^R_{zsCi}	Left and right vertical damping forces at secondary suspension of the *i*th wheelset
F^L_{xai}, F^R_{xai}	Left and right longitudinal forces at anti-hunting dampers of the *i*th bogie
M_{Ri}	Anti-roll torque of the *i*th bogie

Table 3
Notations for the emerging parameters.

Notation	Physical meaning
M_c	Car body mass
R_c	The curvature radius of the track where the car body locates
v	Train speed
r_0	Nominal contact rolling radius of the wheel
ϕ_{sec}	The super elevation angle of the curve high rail where the car body center locates
g	Gravity acceleration
l_c	Half-distance between bogie centers
a_0	Half of track gauge
β_c	The pitch angle of carbody
ψ_c	The yaw angle of carbody
d_s	Half-distance between the secondary suspension of the two sides of the bogie
d_{sc}	Half-distance between the anti- hunting dampers on the two sides of the bogie

and MATLAB/Simulink is established as revealed in Fig. 7.

As for the adams_sub, there are five inputs, which are the damping coefficients of four SLDs and the ideal damping coefficient of *cs*. The lateral speeds of carbody above each SLD (denoted by *vb*), the relative lateral speeds between carbody and each SLD (denoted by *vr*), the lateral carbody acceleration (denoted by *ACCY*), and ECMR (denoted by *W*) are the outputs of the adams_sub. Based on the outputs of the previous simulation step of adams_sub, the inputs for the next simulation step of adams_sub can be calculated by the MATLAB function, which is defined as Eq. (2).

Because the original damping coefficient of SLD is (3.88e + 4) N/(m/s), C_{max} is defined as (3.88e + 4) N/(m/s). Based on previous experience, we define C_{min} as 100 N/(m/s). For better expression, *cs* is defined as $k*C_{max}$. The step size of co-simulation is 0.01 s.

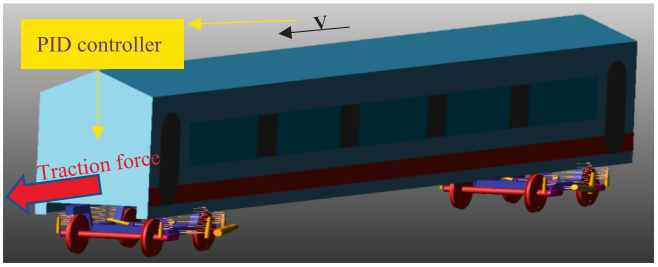

Fig. 5. MBD model of HST.

2.3. Design of running conditions

On one hand, the centrifugal force will aggravate lateral carbody vibration when HST goes through the curved track [44]. On the other hand, ECMR on the curved track is much larger than that on the tangent track [14]. Thus, this paper will investigate the running performance of HST on different curved tracks with different speeds.

According to TB10621-2014 [45], the general curve radius for HSR is between 7000 m and 12000 m. Based on the requirements of [46,47], the superelevation of the curved tracks is set as 150 mm. The track gauge is 1435 mm, and the simulation results through a 1000-meter-length curved track will be collected.

Usually, the minimum and maximum speeds of HST are 250 km/h and 350 km/h respectively considering actual operations [48,49]. Because the optimal value of *k* is between 1 and 1.6 in previous studies [20,23,29], we will test the lateral vibration and energy-consumption indices of HST when its SLDs are controlled by Skyhook strategy whose *k* ranges between 0.2 and 2. The detailed running conditions for simulations are listed in Table 5, where *R* represents curve radius while *v* represents vehicle speed.

Table 4
Track irregularities parameters.

Ω_c (rad · m^{-1})	Ω_r (rad · m^{-1})	Ω_s (rad · m^{-1})	A_a (rad · m)	A_v (rad · m)
0.8246	0.0206	0.4380	2.119E-7	4.032E-7

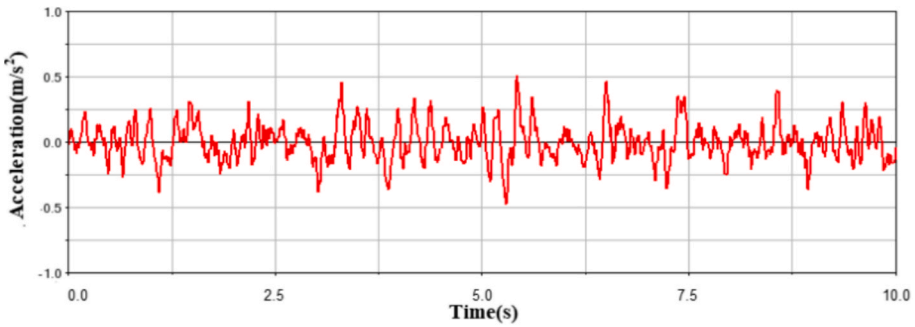

Fig. 6. Lateral acceleration of HST on tangent track.

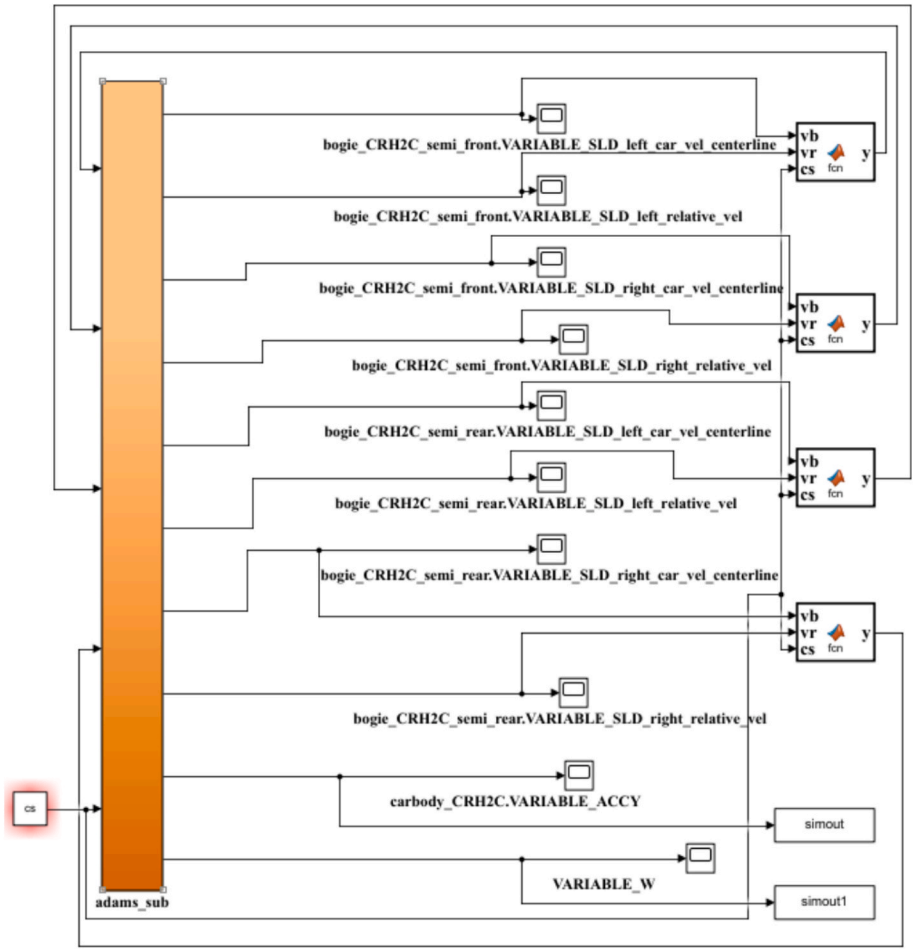

Fig. 7. Simulink model for Skyhook control.

3. Results and discussions

3.1. MBD simulation results

Based on parameter values listed in Table 5, 300 cases are simulated to investigate the roles that k plays in carbody vibration and ECMR of vehicle whose SLDs are integrated with continuous Skyhook controller.

3.1.1. Evaluation of riding comfort

The lateral carbody acceleration in a global coordinate system can reflect riding comfort of a vehicle, and its maximum allowed value is 2.5 m/s^2 [39,50]. As examples, when HST negotiates the curved track with a radius of 7000 m at a speed of 97 m/s, lateral carbody accelerations affected by the value of k are shown in Fig. 8. The peak value of *ACCY* can be used to evaluate the riding comfort.

Table 5
Simulation conditions.

R(m)	7000	8000		9000		10,000		11,000		12,000
v(m/s)	65		73		81		89		97	
k	0.2	0.4	0.6	0.8	1	1.2	1.4	1.6	1.8	2

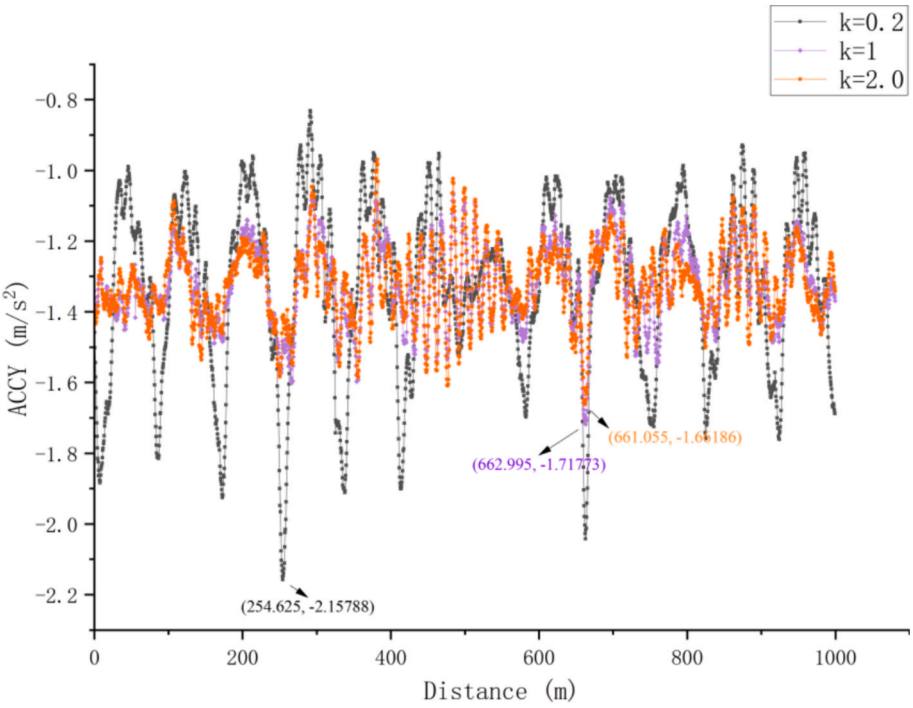

Fig. 8. Lateral carbody vibration of 3 cases.

After all the cases are simulated, the peak lateral carbody accelerations are illustrated in Fig. 9. Obviously, HST with the Skyhook-control SLD can always meet the minimum requirement on riding comfort. Under most circumstances, the carbody vibrates more severely when the curve radius is small due to the impact of centrifugal force. However, if the k is too small, the lateral carbody acceleration can also be at a high level even though the radius is large.

For sake of highlighting effects of k on the riding comfort, Fig. 10 reveals the peak lateral carbody acceleration in the track coordinate system (represented by ACC_{track}) that can be derived based on Eq. (13).

$$ACC_{track} = ACCY - \frac{v^2}{R} \tag{13}$$

Because the maximum lateral acceleration of carbody relative to the track is about 0.5 m/s^2 as introduced in Section 3.1, all the cases whose ACC_{track} is over 0.5 are regarded as unsuccessful attempts and not displayed in Fig. 10.

As illustrated in Fig. 10, the optimal value of k is associated with the curve radius and vehicle speed. With growth of vehicle speed, the curved track with larger radius has better performance in riding comfort. Basically, it is beneficial for the riding comfort to keep k around 1, which is similar with previous studies. But it is necessary to adjust k specifically based on the running conditions to minimize ACC_{track}.

3.1.2. Evaluation of ECMR

By means of Eq. (9), the ECMR can be calculated during simulations. For each simulation case, its ECMR during negotiating the 1000-meter-length curved track is illustrated in Fig. 11. Basically, W decreases sharply before k rises to around 1 and the trend slows down afterwards. Moreover, the minimum values in all the subgraphs demonstrated that the HST with Skyhook-control SLD consumes less energy when it is at high speed. Similar conclusions can be found in [41].

As revealed in Fig. 11, ECMR keeps decreasing gently when k approaches 2. ECMR with larger value of k can only be inferred. Moreover, it is useful to refine the values of k for further improvement in energy saving and vibration isolation. Due to the limited time and computing power, it is difficult to evaluate the performance of HST with every possible k by co-simulations. Consequently, an appropriate regression

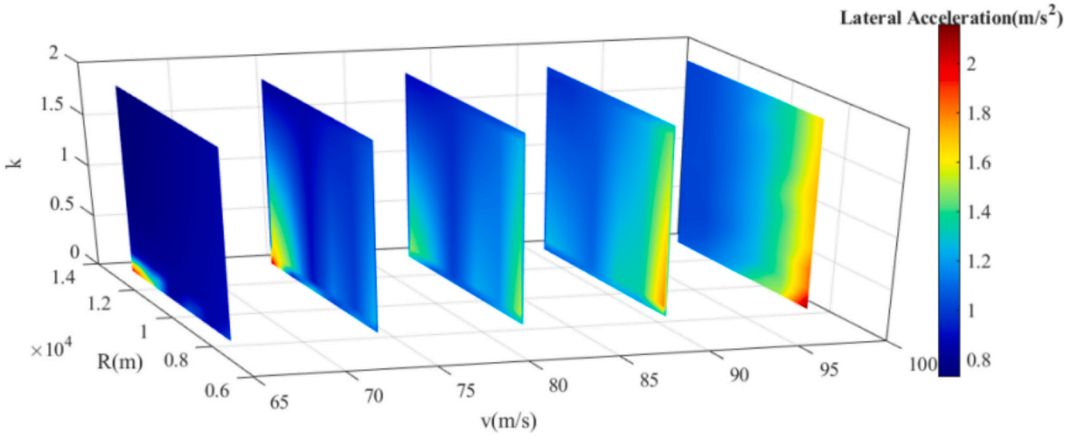

Fig. 9. Simulation results for lateral carbody acceleration.

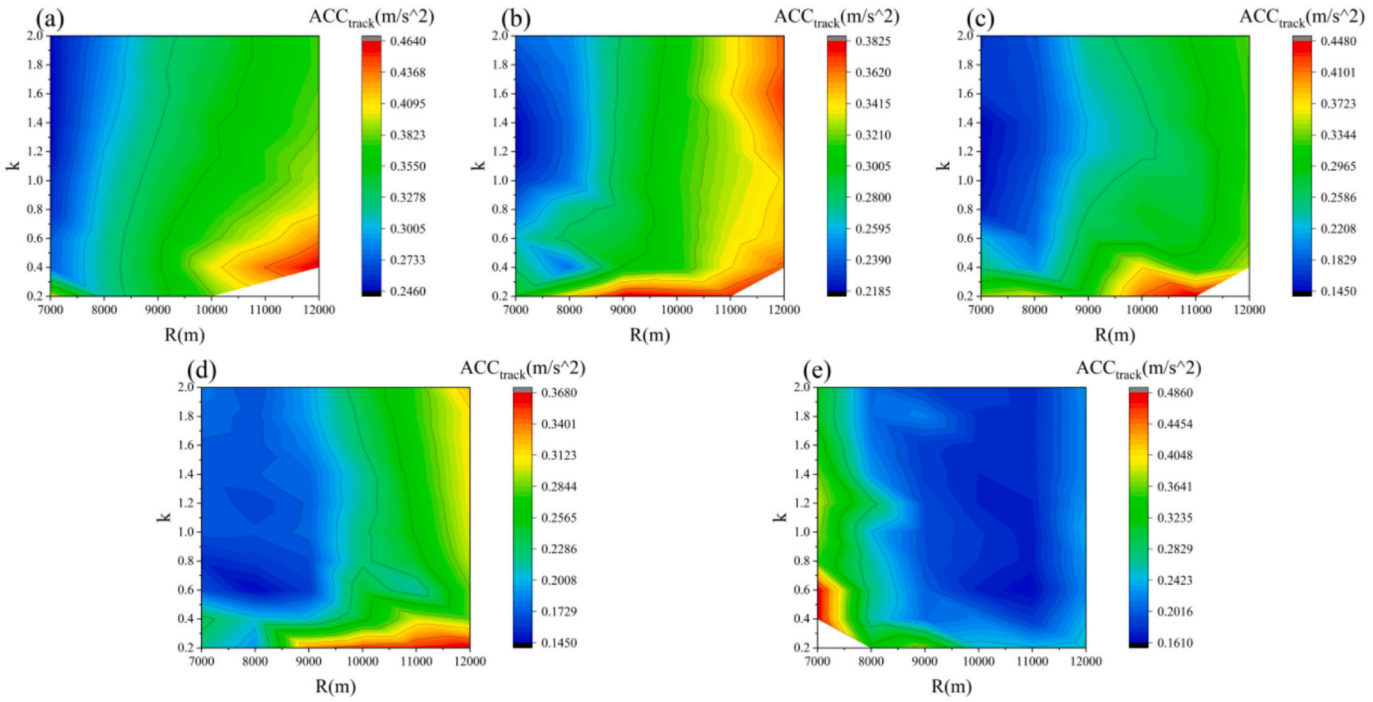

Fig. 10. The lateral vibration of carbody relative to the track: (a) v = 65 m/s, (b) v = 73 m/s, (c) v = 81 m/s, (d) v = 89 m/s, and (e) v = 97 m/s.

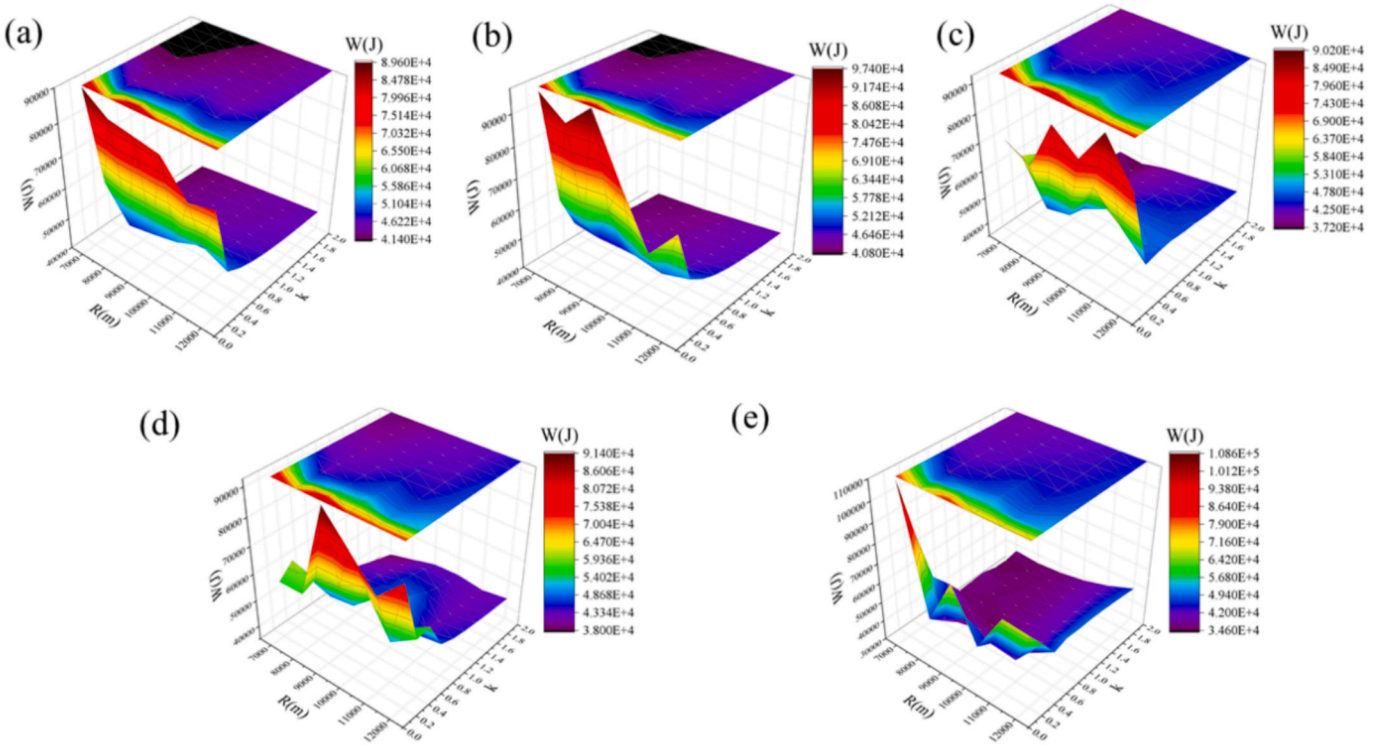

Fig. 11. ECMR of HST through the curved track: (a) v = 65 m/s, (b) v = 73 m/s, (c) v = 81 m/s, (d) v = 89 m/s, and (e) v = 97 m/s.

method needs to be employed to provide a more detailed description of the complex associations between the variables. Through analysis of the simulation data, we find that the effects of k on ACC_{track} and ECMR under different running conditions exhibit diverse nonlinearities, which are difficult to generalize with traditional regression methods. By contrast, the latest developments in deep learning have demonstrated the potential of this technology to be a highly effective tool with applications across a range of domains. It offers substantial advantages in terms of computational power, parallelization, and accuracy when solving intricate nonlinear problems [51]. Thus, we hope to establish the deep learning model to reveal effects of k on ACC_{track} and ECMR in a broad range.

3.2. Regression functions by CNN

CNN is one of the most significant networks in the deep learning

field, which is capable of modeling nonlinear responses and extracting hidden features from raw data [52]. It has been shown to outperform classical machine learning models with respect to accuracy and robustness [53]. In particular, CNN processes all input dimensions simultaneously via convolutional operations, making them faster to train than recurrent neural network (RNN), which suffers from sequential dependency and vanishing gradients [54]. Meanwhile, CNN shares weights across spatial locations, reducing the risk of overfitting compared to fully connected networks or machine learning methods, which scale poorly with high-dimensional data [55]. Moreover, from the analysis in Section 3.1, we find that k, vehicle speed, and curve radius exhibit grid-like spatial correlations when mapped to ACC_{track} and ECMR. In contrast to RNN, which is engineered for sequential data and would inefficiently model these geometric relationships, CNN excels at capturing local spatial dependencies through the use of convolutional filters. In light of the aforementioned characteristics, a CNN regression model is constructed in this study to further explore the roles that k, vehicle speed, and curve radius play in riding comfort and energy consumption.

3.2.1. CNN configurations

A typical CNN architecture is the stack of convolutional layers, pooling layers, and fully-connected layers [56]. Convolutional layers comprise a set of learnable kernel filters that enable the feature extraction of input data. After acquiring the convolved output, neurons often undergo an activation operation to introduce nonlinearity in the network. The pooling operation filters some features of the convolutional layer to realize data dimensionality reduction and accelerate parameter convergence. Several fully-connected layers bring the CNN architecture to an end for performing the regression task.

Considering the characteristics of the simulation data, the proposed CNN model is configured with 2 convolutional layers, 2 pooling layers, and 2 fully-connected layers, as depicted in Fig. 12. Inputs to this network are curve radius, vehicle speed, and k, and outputs are ACC_{track} and ECMR. For convolutional layers, the kernel size is set to 64×1 with stride as 1. The Rectified linear unit (ReLU) is applied as the non-linear activation function.

3.2.2. Training process and performance evaluation

The objective of training process is optimizing the parameters of the layers' filters to minimize a specific loss function. In this paper, the mean square error (MSE) is selected as the loss function to assess the output layer's error. We partition 80 % of the simulation results randomly as the training set, reserving the remaining 20 % for testing purposes. Data processing is implemented using the MATLAB programming language.

The network performance is evaluated using the test set, which remains independent throughout the training phase. Fig. 13 provides the comparison of actual and predicted values of ACC_{track} and ECMR. It can be noted that the predictions and observed values are strongly in agreement.

To quantitatively assess model performance, we adopt two common metrics, i.e., R-square (R^2) and mean absolute percentage error (MAPE), which can be calculated based on Eqs. (14) and (15). The R^2 and MAPE for ACC_{track} are 0.96 and 4.9 %, and those for ECMR are 0.94 and 3.4 %, respectively. It confirms the high accuracy of the proposed CNN model.

$$R^2 = 1 - \frac{\sum_{k=1}^{N}(y_k - \widehat{y}_k)^2}{\sum_{k=1}^{N}(y_k - \bar{y})^2} \tag{14}$$

$$MAPE = \frac{1}{N}\sum_{k=1}^{N}\left|\frac{\widehat{y}_k - y_k}{y_k}\right| \tag{15}$$

where N represents the data volume, y_k and $\widehat{y}_k$ represent the actual and predicted values, respectively, $\bar{y}$ represents the mean of all actual values.

3.3. Bi-objective optimization of Skyhook controller

For sake of balancing vibration isolation and energy consumption, we propose a bi-objective optimizing problem by adjusting k of Skyhook controller. ACC_{track} and ECMR are selected as optimization objectives, both of which should be minimized.

3.3.1. Model formulation

According to the CNN regression model, ACC_{track} and ECMR of HST under various running conditions are calculated, as shown in Fig. 14. With k ranging from 0.2 to 15, ECMR generally declines, while the opposite is true for ACC_{track}. Therefore, ACC_{track} and ECMR can be chosen as two conflicting objectives, formulated by Eqs. (16) and (17).

$$Objfun_1 = min[net\_ACC(v, R, k)] \tag{16}$$

$$Objfun_2 = min[net\_ECMR(v, R, k)] \tag{17}$$

where $net\_ACC(\bullet)$ and $net\_ECMR(\bullet)$ denote the CNN regression functions for ACC_{track} and ECMR, respectively, v denotes the vehicle speed, R denotes the curve radius, k denotes the scale factor of the Skyhook control strategy.

To get a more detailed insight into the trends of ACC_{track} and ECMR with varying k, Fig. 15 and Fig. 16 display the relationship between k and ACC_{track} as well as ECMR for various curve radii. Apparently, when k exceeds 10, ACC_{track} tends to be greater than 0.5 and the downtrend of ECMR becomes flat. As a result, the value of k in this model is restricted by Eq. (18).

3.3.2. Solving approach and optimization results

According to Eqs. (16)-(18), the bi-objective optimization model of Skyhook controller can be constructed. Since values of the objective functions basically contradict, the goal of optimization is to obtain the Pareto optimal set that satisfies each objective. In this paper, NSGA-II is adopted to search for Pareto optimal solutions on MATLAB platform. NSGA-II has been extensively employed in mechanical system optimization due to advantages such as high speed and good convergence [57–59]. It incorporates fast non-dominated sorting and crowding distance mechanisms, which reduce computational complexity while maintaining diversity among solutions [60]. This is beneficial for the high-dimensional input space derived from the CNN regression model. Furthermore, NSGA-II is adept at handling nonlinear relationships [61], making it suitable for optimizing the CNN-predicted responses of ACC_{track} and ECMR, which exhibit highly nonlinear dependencies on k, vehicle speed, and curve radius.

The optimization process is conducted using MATLAB R2020b on a PC equipped with an Intel Core i5-13500H processor (3.19 GHz) and 32 GB of RAM. In order to achieve comprehensive exploration of the search space and identify the optimal configuration for minimizing the objective functions, multiple executions of NSGA-II are conducted with systematic variations of its critical parameters. Following 300 generations of optimization, the best-performing parameter combination was determined, as detailed in Table 6. For each vehicle speed and curve radius, the computation takes approximately 70 min to complete.

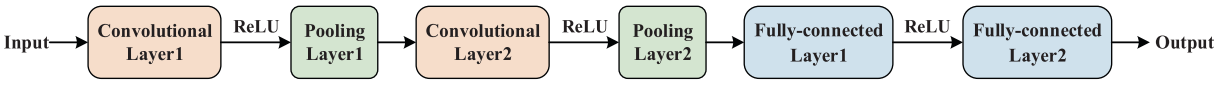

Fig. 12. Proposed CNN structure.

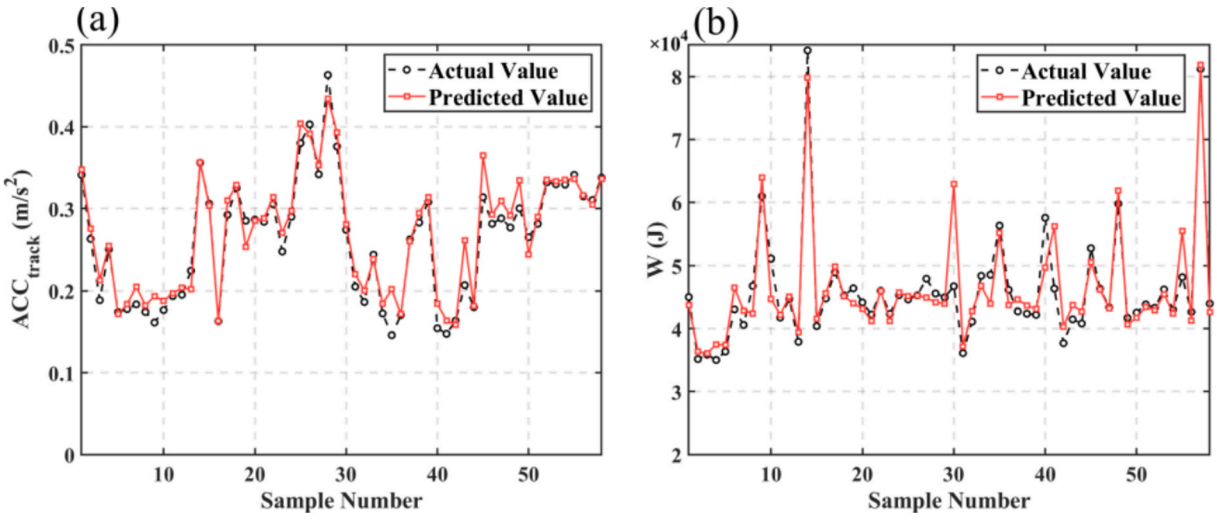

Fig. 13. Comparison of actual and predicted values: (a) ACC_{track} and (b) ECMR.

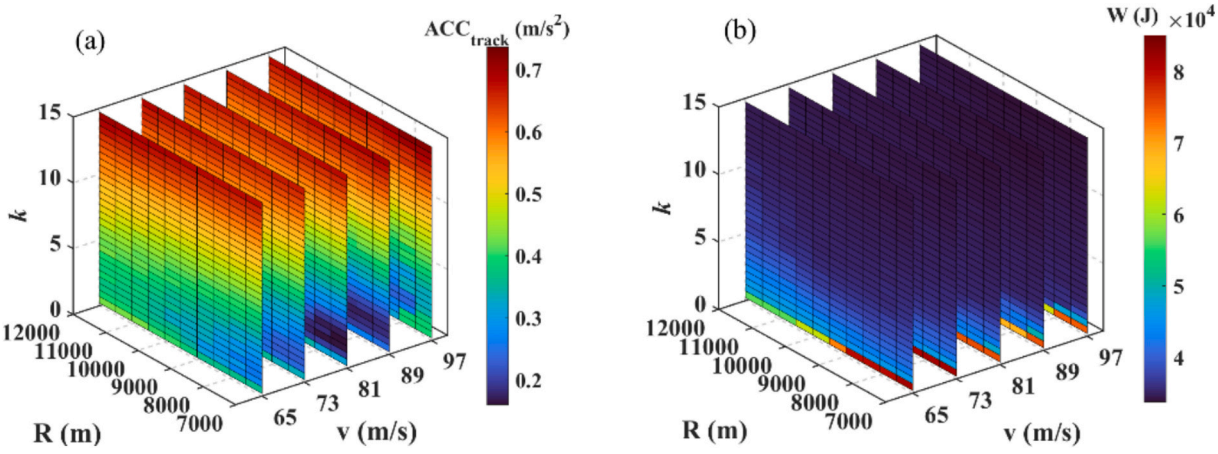

Fig. 14. CNN regression results: (a) ACC_{track} and (b) ECMR.

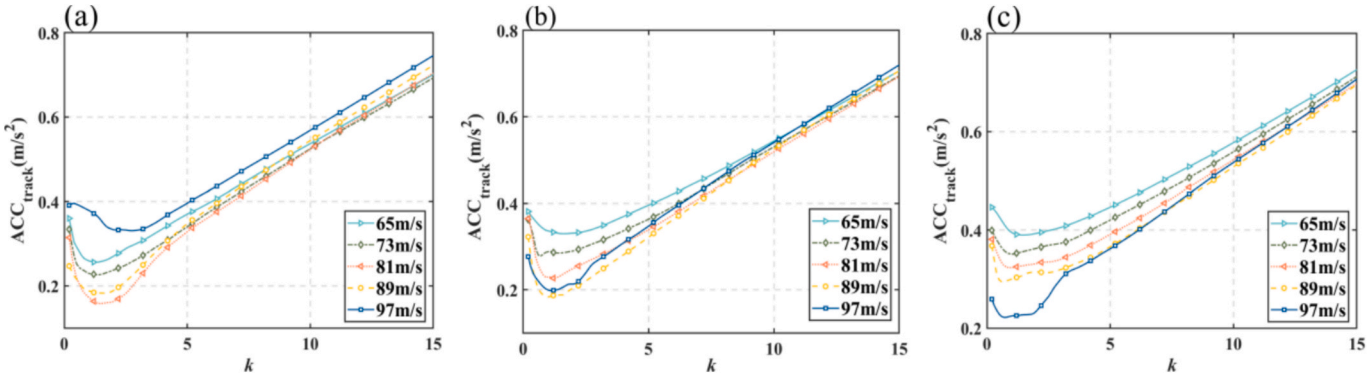

Fig. 15. ACC_{track} for different curve radii: (a) $R = 7000$ m, (b) $R = 9000$ m, and (c) $R = 12000$ m.

Although the initial optimization requires significant computational time, the Pareto optimal solutions obtained can be stored offline and retrieved quickly in practical applications. This enables real-time adjustment of the scale factor of k, tailored to specific requirements for riding comfort and energy consumption. Consequently, efficient and responsive control of the suspension system is ensured under varying operational conditions.

Pareto fronts under different curve radii and vehicle speeds are shown in Fig. 17. For comparative analysis, we also mark the corresponding objective values when the passive control strategy is applied for the same running scenario, which means the damping coefficient of SLD remains constant. Taking Fig. 17(a) and (b) as examples, the solutions denoted within the red, green, and pink circles are termed as the preferred solutions, the comfort-optimal solution, and the energy-optimal solution at a speed of 65 m/s, respectively. The associated values of k are revealed in Fig. 18. In contrast to the passive control,

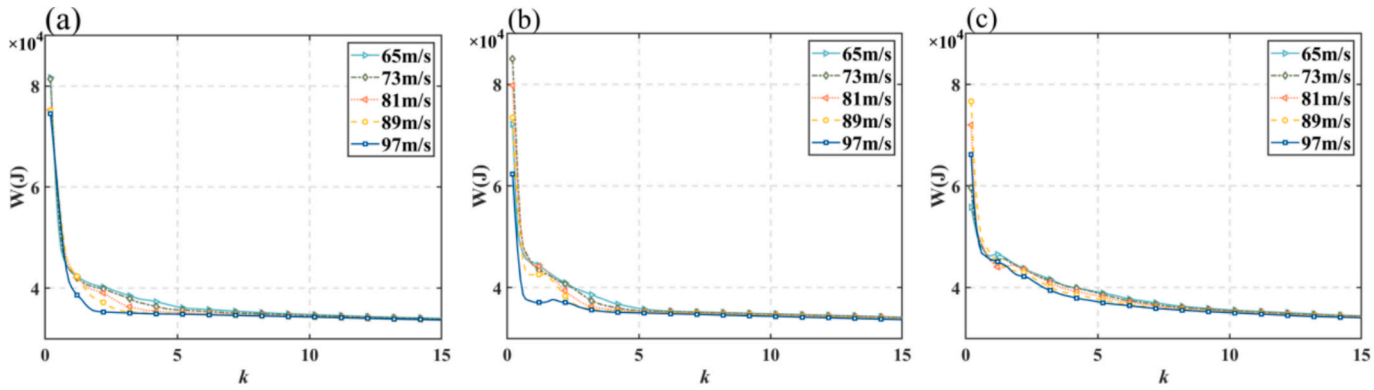

Fig. 16. ECMR for different curve radii: (a) $R = 7000$ m, (b) $R = 9000$ m, and (c) $R = 12000$ m.

Table 6
NSGA-II algorithm parameter settings.

Parameters	Value
Population size	200
Crossover percentage	0.8
Mutation percentage	0.2
Maximum number of iterations	300

preferred solutions can enhance both vibration isolation and energy efficiency. For the comfort-optimal and energy-optimal solution, they are capable of minimizing one optimization objective without adversely affecting the other.

By comparison with passive control strategy, the average percentage reduction of preferred solutions in ACC_{track} and ECMR is illustrated in Fig. 19. It is proved that the adjustable Skyhook control strategy can reduce ACC_{track} and ECMR by up to 47.78 % and 15.90 %, respectively. The effectiveness of Skyhook controller basically enhances with increasing vehicle speed.

Fig. 20 depicts the percentage decrease in ACC_{track} for the comfort-optimal solution and ECMR for the energy-optimal solutions. Without jeopardizing energy consumption, the comfort-optimal solution can improve riding comfort by up to 64.25 %. Besides, a maximum energy consumption savings of 25.56 % can be achieved through the energy-optimal solution.

However, the aforementioned three types of solutions are not available when $R = 11000$ m, $v = 65$ m/s and $R = 12000$ m, $v = 65$ m/s. As can be inferred from Fig. 17(e) and (f), all the Pareto optimal solutions cannot effectively decrease ACC_{track} if there is no more energy consumption. For these cases when the vehicle cruises at low speed on large radius curves, the centrifugal acceleration is small and the requirement for lateral riding comfort is low. Thus, the optimization of the Skyhook control can focus on saving energy.

In summary, we suggest adjusting the control strategy based on the vehicle speed and curve radius. When the Skyhook control strategy is

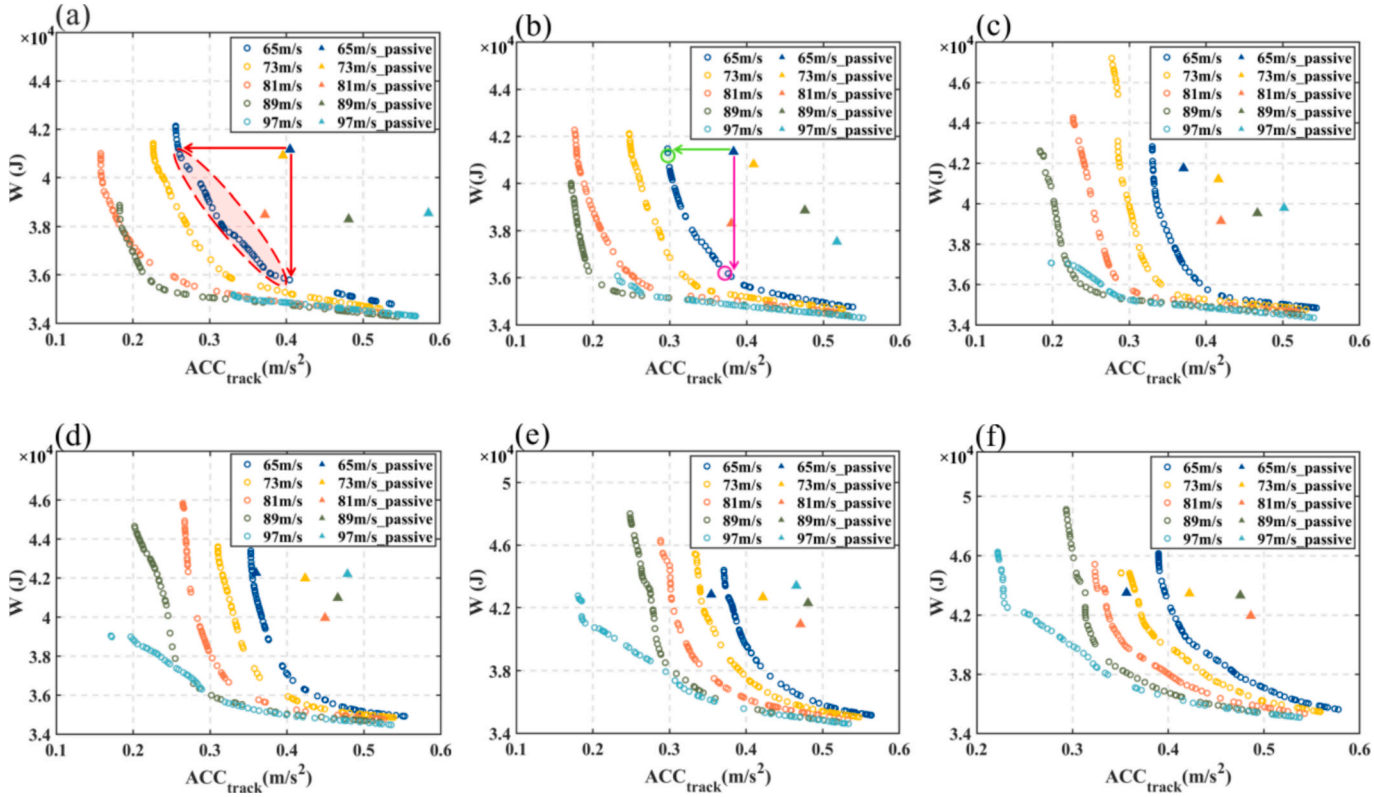

Fig. 17. Pareto fronts for different curve radii: (a) $R = 7000$ m, (b) $R = 8000$ m, (c) $R = 9000$ m, (d) $R = 10000$ m, (e) $R = 11000$ m, and (f) $R = 12000$ m.

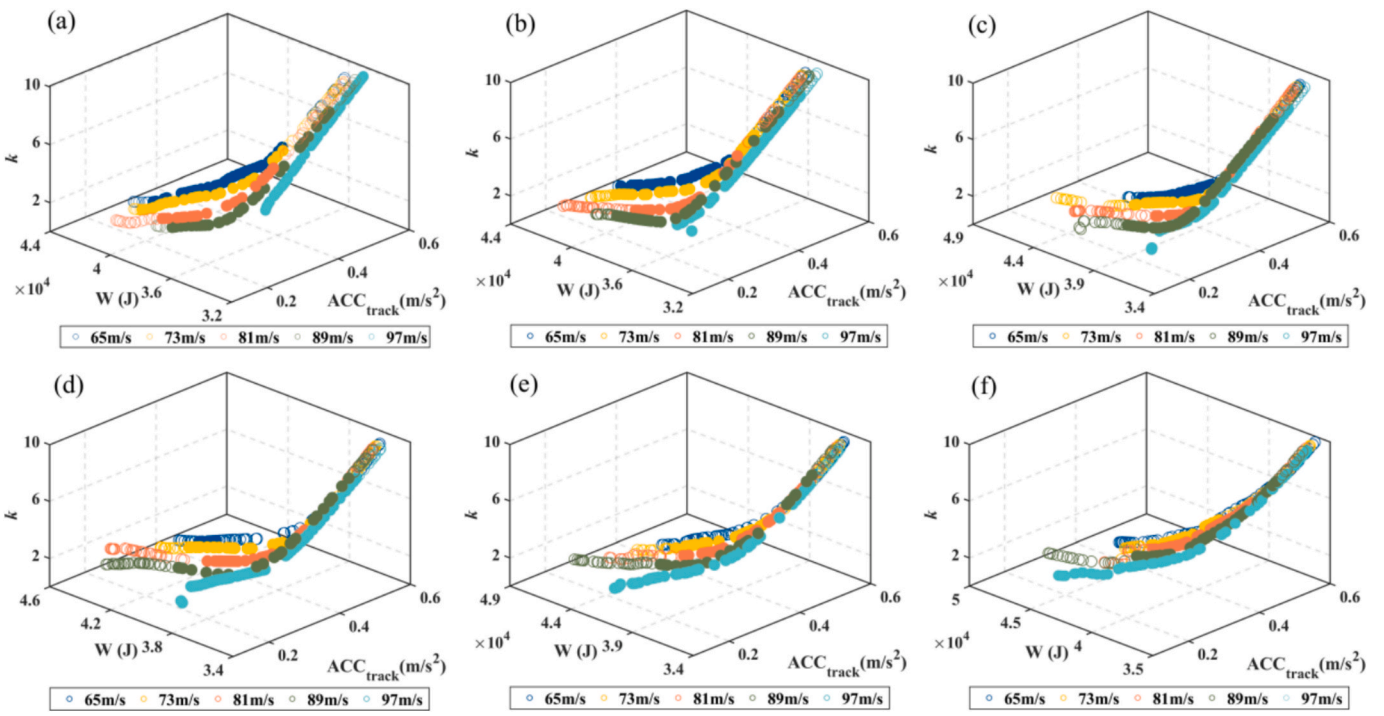

Fig. 18. Pareto optimal values of k for different curve radii: (a) R = 7000 m, (b) R = 8000 m, (c) R = 9000 m, (d) R = 10000 m, (e) R = 11000 m, and (f) R = 12000 m.

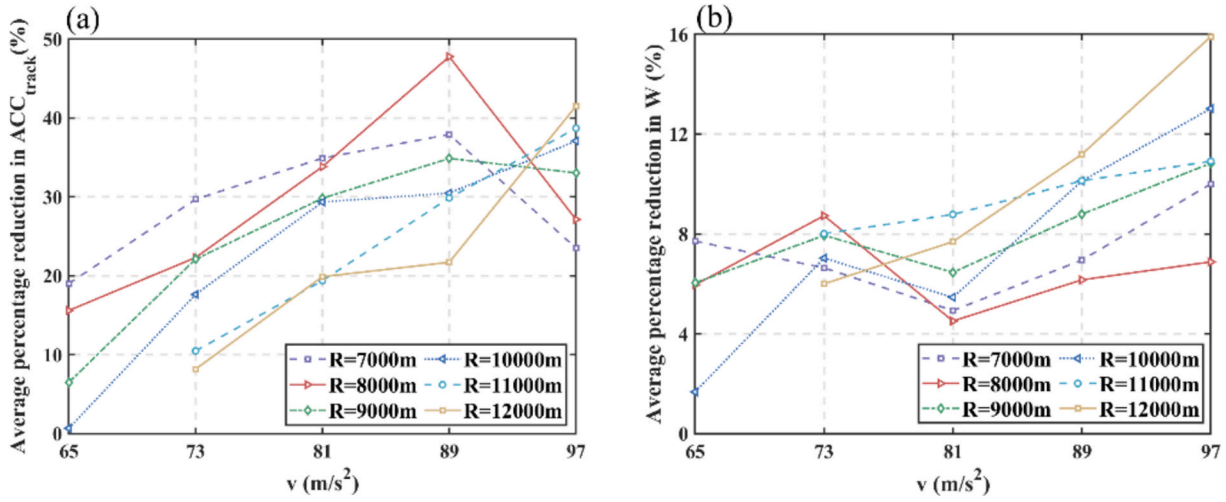

Fig. 19. Average percentage reduction for preferred solutions compared to the passive control: (a) ACC_{track} and (b) ECMR.

adopted, preferred solutions should be given priority to, and the comfort-optimal and energy-optimal solutions can be accepted if the riding comfort or energy efficiency is emphasized.

4. Conclusions

In this study, the CNN driven control strategy of SLD is proposed by modifying the original skyhook strategy to improve energy efficiency and vibration isolation of HST on curved tracks. According to co-simulation results, a CNN regression model is constructed for deriving Pareto optimal solutions of the scale factor (denoted by k). The main conclusions drawn from this study are as follows:

(1) By means of co-simulation between VI-Rail and MATLAB/Simulink, k is proved to play different roles in energy consumption and vibration isolation of HST on curved tracks. From the perspective of reducing the lateral vibration of carbody, k should be around 1. But ECMR keeps decreasing when k is larger than 1. Thus, we need to improve the value of k if we want to conserve energy.

(2) It is necessary to adjust the value of k according to the running conditions. Based on the co-simulation results, a CNN regression model is built to reveal the roles that k, vehicle speed, and curve radius play in carbody vibration and energy consumption. Due to the different effects of k on ACC_{track} and ECMR, NSGA-II is used to derive Pareto fronts under various running conditions. It is strongly recommended to adopt the corresponding preferred solutions in different running conditions because these values of k can enhance both energy efficiency and vibration isolation, compared to the passive control strategy.

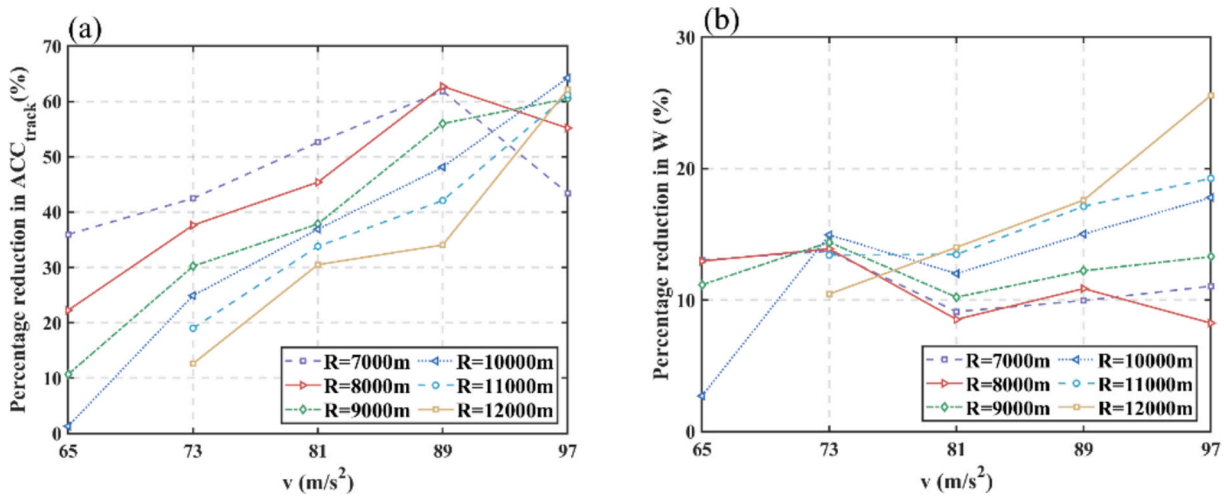

Fig. 20. Percentage reduction compared to the passive control: (a) ACC_{track} with comfort-optimal solutions and (b) ECMR with energy-optimal solutions.

(3) Although the preferred solutions have priority, the comfort-optimal and energy-optimal solutions respectively have significant effects on improving the vibration isolation and energy efficiency. By contrast with the passive control strategy, preferred solutions can respectively decrease ACC_{track} and ECMR by up to 47.78 % and 15.90 % on average. By contrast, the comfort-optimal solution can improve riding comfort by up to 64.25 %, and at most 25.56 % of ECMR can be saved by the energy-optimal solution, on the premise of not making the other index worse.

In the future, we plan to improve the CNN driven control strategy of SLD considering the phases of vehicle coasting, accelerating, and braking to develop a smarter suspension applicable for any running status. Additionally, this study assumes the ideal physical state for the Skyhook controller. To bridge the gap between simulation and real-world deployment, subsequent research will integrate time-delay effects and nonlinear damping characteristics into the co-simulation and optimization framework and validate the control algorithm under hardware-in-the-loop conditions with a variety of commercial dampers.

CRediT authorship contribution statement

Duo Zhang: Writing – original draft, Software, Methodology, Conceptualization. **Hong-Wei Li:** Writing – review & editing. **Fang-Ru Zhou:** Writing – review & editing, Visualization, Investigation. **Yin-Ying Tang:** Validation, Resources, Formal analysis, Data curation. **Qi-Yuan Peng:** Supervision, Project administration, Funding acquisition.

Declaration of competing interest

The authors declare that they have no known competing financial interests or personal relationships that could have appeared to influence the work reported in this paper.

Acknowledgement

This research was supported by the National Key Research and Development Program of China [grant number 2022YFB4300502]. The authors would also like to appreciate the funding supported by European Union's Horizon Europe Program for Marie Skłodowska-Curie Actions under Grant TEESFtrain [grant number 101198179].

Data availability

Data will be made available on request.

References

[1] Islam ZU, Lipu MH, Karim TF, Fuad AM, Ali MN, Shihavuddin ASM, et al. Optimizing hybrid renewable energy based automated railway level crossing in Bangladesh: techno-economic, emission and sensitivity analysis. Energy Convers Manage: X 2024;24:100744.
[2] Azmi R, Mirzaei M, Habibzadeh-Sharif A. A novel optimal control strategy for regenerative active suspension system to enhance energy harvesting. Energy Convers Manage 2023;291:117277.
[3] Deng K, Fang T, Feng H, Peng H, Löwenstein L, Hameyer K. Hierarchical eco-driving and energy management control for hydrogen powered hybrid trains. Energy Convers Manage 2022;264:115735.
[4] Douglas H, Roberts C, Hillmansen S, Schmid F. An assessment of available measures to reduce traction energy use in railway networks. Energy Convers Manage 2015;106:1149–65.
[5] Li C, Liu M, Chang R, Wang X, Liu W, Zhang H. Air pressure and comfort study of the high-speed train passing through the subway station. Sustain Cities Soc 2022;81:103881.
[6] Howlett PG, Milroy IP, Pudney PJ. Energy-efficient train control. Control Eng Pract 1994;2:193–200.
[7] Sun X, Lu H, Dong H. Energy-efficient train control by multi-train dynamic cooperation. IEEE T Intell Transp 2017;18:3114–21.
[8] Fernández-Rodríguez A, Fernández-Cardador A, Cucala AP. Balancing energy consumption and risk of delay in high speed trains: a three-objective real-time eco-driving algorithm with fuzzy parameters. Transp Res Pt C-Emerg Technol 2018;95:652–78.
[9] Xing Z, Zhang Z, Guo J, Qin Y, Jia L. Rail train operation energy-saving optimization based on improved brute-force search. Appl Energy 2023;330:120345.
[10] Wang P, Trivella A, Goverde RM, Corman F. Train trajectory optimization for improved on-time arrival under parametric uncertainty. Transp Res Pt C-Emerg Technol 2020;119:102680.
[11] Hemida H. Contribution of computational wind engineering in train aerodynamics—past and future. J Wind Eng Ind Aerodyn 2023;234:105352.
[12] Mistry PJ, Johnson MS, Galappaththi U. Selection and ranking of rail vehicle components for optimal lightweighting using composite materials. Proc Inst Mech Eng Part F-J Rail Rapid Transit 2021;235:390–402.
[13] Carruthers JJ, Calomfirescu M, Ghys P, Prockat J. The application of a systematic approach to material selection for the lightweighting of metro vehicles. Proc Inst Mech Eng Part F-J Rail Rapid Transit 2009;223:427–37.
[14] Zhang D, Tang Y, Peng Q. A novel approach for decreasing driving energy consumption during coasting and cruise for the railway vehicle. Energy 2023;263:125615.
[15] Gijón-Rivera C, Olazagoitia JL, Reyes-Avendaño JA. Design and development of a novel Four-Links rotational hybrid Energy-Harvesting suspension system compatible with conventional suspension technologies. Energy Convers Manage X 2024;22:100572.
[16] Zhao Y, Liu Y, Yang S, Liao Y, Chen Z. Analysis on new semi-active control strategies to reduce lateral vibrations of high-speed trains by simulation and hardware-in-the-loop testing. Proc Inst Mech Eng Part F-J Rail Rapid Transit 2022;236:960–72.
[17] Leblebici AS, Türkay S. An H∞ and skyhook controller design for a high speed railway vehicle. IFAC-PapersOnLine 2018;51:156–61.
[18] Wang C, Cui X, Zhao S, Zhou X, Song Y, Wang Y, et al. Enhancing vehicle ride comfort through deep reinforcement learning with expert-guided soft-hard constraints and system characteristic considerations. Adv Eng Inf 2024;59:102328.
[19] Zhang C, Kordestani H, Shadabfar M. A combined review of vibration control strategies for high-speed trains and railway infrastructures: challenges and solutions. J Low Freq Noise Vib Act Control 2023;42:272–91.

[20] Wu Y, Gan F, Shi H, Zeng J, Chen C, Feng Y. Experimental investigations on the semi-active control of a valve-driven secondary lateral damper for a high-speed rail vehicle. J Vib Control 2023;29:3025–37.
[21] Stribersky A, Kienberger A, Wagner G, Müller H. Design and evaluation of a semi-active damping system for rail vehicles. Veh Syst Dyn 1998;29:669–81.
[22] Oishi T, HAYASHI T, Sasaki K, Arai J. A502 development of advanced semi-active suspension system for shinkansen vehicles. In: The Proceedings of International Symposium on Seed-up and Service Technology for Railway and Maglev Systems: STECH. 2003, p. 220-4.
[23] Zhao Y, Liu Y, Yang S, Liao Y, Li Y. A new coordination control strategy on secondary lateral damper for high-speed trains. J Vib Eng Technol 2022;10:395–408.
[24] Goodall R, Freudenthaler G, Dixon R. Hydraulic actuation technology for full-and semi-active railway suspensions. Veh Syst Dyn 2014;52:1642–57.
[25] Wang X, Liu B, Di Gialleonardo E, Kovacic I, Bruni S. Application of semi-active yaw dampers for the improvement of the stability of high-speed rail vehicles: mathematical models and numerical simulation. Veh Syst Dyn 2022;60:2608–35.
[26] Fu B, Liu B, Di Gialleonardo E, Bruni S. Semi-active control of primary suspensions to improve ride quality in a high-speed railway vehicle. Veh Syst Dyn 2023;61:2664–88.
[27] Guo J, Xu Z, Sun Y. A new semi-active safety control strategy for high-speed railway vehicles. Veh Syst Dyn 2015;53:1918–34.
[28] Jean P, Ohayon R, Le Bihan D. Semi-active control using magneto-rheological dampers for payload launch vibration isolation. In: Smart Structures and Materials 2006: Damping and Isolation 6169. 2006, p. 113-22.
[29] Oh J, Shin Y, Koo H, Kim H, Park J, Choi S. Vibration control of a semi-active railway vehicle suspension with magneto-rheological dampers. Adv Mech Eng 2016;8:756501962.
[30] Balaji PA, Sugumaran V. Comparative study of machine learning and deep learning techniques for fault diagnosis in suspension system. J Braz Soc Mech Sci Eng 2023;45(4):215.
[31] Konoiko A, Kadhem A, Saiful I, Ghorbanian N, Zweiri Y, Sahinkaya MN. Deep learning framework for controlling an active suspension system. J Vib Control 2019;25(17):2316–29.
[32] Zhang W, Ji H. High stability control of a magnetic suspension flywheel based on SA-BPNN and CNN+ LSTM+ ATTENTION. Machines 2024;12(10):710.
[33] Li M, Lv G, Wang X, Yue T. High-speed maglev train suspension gap prediction based on CNN-AGCRN. In: 2024 5th International Conference on Machine Learning and Computer Application; 2024. p. 425–30.
[34] Ye Y, Huang P, Zhang Y. Deep learning-based fault diagnostic network of high-speed train secondary suspension systems for immunity to track irregularities and wheel wear. Railway Eng Sci 2022;30:96–116.
[35] Sun J, Cong J. Deep learning based road recognition for intelligent suspension systems. J Theor Appl Mech 2021;59(3).
[36] Jin T, Liu Z, Sun S, Ren Z, Deng L, Yang B, et al. Development and evaluation of a versatile semi-active suspension system for high-speed railway vehicles. Mech Syst Signal Proc 2020;135:106338.
[37] Liao Y, Liu Y, Yang S. Semiactive Control of high-speed railway vehicle suspension systems with magnetorheological dampers. Shock Vib 2019;2019(1):5279380.
[38] Zhang D, Tang Y, Peng Q, Dong C, Ye Y. Effect of mass distribution on curving performance for a loaded wagon. Nonlinear Dyn 2021;104:2259–73.
[39] Zhai W. Vehicle-track coupled dynamics: theory and applications. Springer Nature; 2019.
[40] Borase RP, Maghade DK, Sondkar SY, Pawar SN. A review of PID control, tuning methods and applications. Int J Dyn Control 2021;9(2):818–27.
[41] Zhang D, Zhou F, Tang Y, Tao Z, Peng Q. Optimization of the loading plan for a railway wagon from the perspectives of running safety and energy conservation. Energy 2023;280:128229.
[42] Zhai W, Liu P, Lin J, Wang K. Experimental investigation on vibration behaviour of a CRH train at speed of 350 km/h. Int J Rail Transp 2015;3:1–16.
[43] Bahn D. Lastenheft IC-express. Munich: BZA; 1993.
[44] Zhang D, Tang Y, Clarke DB, Peng Q, Dong C. An innovative method for calculating diagonal lashing force of cargo on railway wagons in a curve alignment. Veh Syst Dyn 2019;59(3):352–74.
[45] Ministry of Railways of China. TB10621-2014: Code for design of high-speed railway. 2014.
[46] British Standards Institution. BS EN 14363: 2016 Railway Applications-Testing and Simulation for the Acceptance of Running Characteristics of Railway Vehicles-Running Behaviour and Stationary Tests. 2016.
[47] British Standards Institution. BS EN 13803: 2017 Railway Applications-Track-Track Alignment Design Parameters-Track Gauges 1 435 mm and Wider. 2017.
[48] Wei Y, Sun K, Zhong X, Jia J, Huang Q, Qin J, et al. Study on effects of the train-induced airflow on the temperature field of high-speed railway tunnels in cold regions. Therm Sci Eng Prog 2023;41:101837.
[49] Chen H, Deng Y, Xu S. Study on optimal design of simply-supported box beam with 32 m span in high-speed railway. Railway Standard Design 2023;67(9).
[50] International Union of Railways. UIC 518-2005 Testing and approval of railway vehicles from the point of view of their dynamic behaviour - Safety - Track fatigue - Ride quality. 2005.
[51] Tahir MF, Tzes A, Yousaf MZ. Enhancing PV power forecasting with deep learning and optimizing solar PV project performance with economic viability: a multi-case analysis of 10 MW Masdar project in UAE. Energy Convers Manage 2024;311:118549.
[52] Li Z, Liu F, Yang W, Peng S, Zhou J. A survey of convolutional neural networks: analysis, applications, and prospects. IEEE Trans Neural Netw Learn Syst 2021;33(12):6999–7019.
[53] Yaghoubirad M, Azizi N, Farajollahi M, Ahmadi A. Deep learning-based multistep ahead wind speed and power generation forecasting using direct method. Energy Convers Manage 2023;281:116760.
[54] Kow PY, Wang YS, Zhou Y, Kao IF, Issermann M, Chang LC, et al. Seamless integration of convolutional and back-propagation neural networks for regional multi-step-ahead PM2.5 forecasting. J Clean Prod 2020;261:121285.
[55] Huo W, Li W, Zhang Z, Sun C, Zhou F, Gong G. Performance prediction of proton-exchange membrane fuel cell based on convolutional neural network and random forest feature selection. Energy Convers Manage 2021;243:114367.
[56] Ali S, Waleed M, Lee D. A novel AI-based CNN model to predict the structural performance of monopile used for offshore wind energy systems. Energy Convers Manage X 2025;26:101028.
[57] Koç MA. A new expert system for active vibration control (AVC) for high-speed train moving on a flexible structure and PID optimization using MOGA and NSGA-II algorithms. J Braz Soc Mech Sci Eng 2022;44(4):151.
[58] Zhang J, Hu G, Yang C, Yu L, Zhu W. NSGA-II-TLQR Control of semi-active suspension system with magnetorheological damper considering response time delay. J Vib Eng Technol 2024;12:825–38.
[59] Kong F, Liu Z, Lin C, Wang Z, Wang W, Yao S, et al. Experimental study and parameter optimization of desiccant wheel-assisted atmospheric water harvesting system based on NSGA-II. Energy Convers Manage 2025;339:119943.
[60] Khan TE, Sakib SH, Sakib N, Hossain T, Ehsan MM, Khan Y. Multi-Objective optimization of a cascaded supercritical CO_2 brayton cycle with ejector-enhanced transcritical CO_2 and flash tank absorption refrigeration cycles. Energy Convers Manage X 2025;26:100988.
[61] Bakhshinezhad S, Mohebbi M. Multi-objective optimal design of semi-active fluid viscous dampers for nonlinear structures using NSGA-II. Structures 2020;24:678–89.